Monthly Notices
of the
ROYAL ASTRONOMICAL SOCIETY
MNRAS **491,** 4894–4901 (2020) doi:10.1093/mnras/stz2853

Azimuthal variations of oxygen abundance profiles in star-forming regions of disc galaxies in EAGLE simulations

Martín Solar,[1] Patricia B. Tissera [2]★ and Jose A. Hernandez-Jimenez[2]
[1]*Instituto de Física y Astronomía, Facultad de Ciencias, Universidad de Valparaíso, Gran Bretaña 1111, Valparaíso, Chile*
[2]*Departamento de Ciencias Físicas, Universidad Andrés Bello, 700 Fernández Concha, Las Condes, Santiago, Chile*

Accepted 2019 October 5. Received 2019 October 1; in original form 2019 August 16

ABSTRACT

The exploration of the spatial distribution of chemical abundances in star-forming regions of galactic discs can help us to understand the complex interplay of physical processes that regulate the star formation activity and the chemical enrichment across a galaxy. We study the azimuthal variations of the normalized oxygen abundance profiles in the highest numerical resolution run of the Evolution and Assembly of GaLaxies and their Environments (EAGLE) Project at $z = 0$. We use young stellar populations to trace the abundances of star-forming regions. Oxygen profiles are estimated along different line of sights from a centrally located observer. The mean azimuthal variation in the EAGLE discs are $\sim$0.12 $\pm$ 0.03 dex $R_{\rm eff}^{-1}$ for slopes and $\sim$0.12 $\pm$ 0.03 dex for the zero-points, in agreement with previous works. Metallicity gradients measured along random directions correlate with those determined by averaging over the whole discs, although with a large dispersion. We find a slight trend for higher azimuthal variations in the disc components of low star-forming and bulge-dominated galaxies. We also investigate the metallicity profiles of stellar populations with higher and lower levels of enrichment than the average metallicity profiles, and we find that high star-forming regions with high metallicity tend to have slightly shallower metallicity slopes compared with the overall metallicity gradient. The simulated azimuthal variations in the EAGLE discs are in agreement with observations, although the large variety of metallicity gradients would encourage further exploration of the metal mixing in numerical simulations.

Key words: galaxies: abundances – galaxies: evolution – galaxies: ISM.

1 INTRODUCTION

The standard model for disc formation proposed by Fall & Efstathiou (1980) is based on the hypothesis of specific angular momentum conservation of the gas as it cools. Numerical simulations have shown that if the condition of angular momentum conservation is globally fulfilled, discs that satisfy the observed scale relations are formed (e.g. Pedrosa & Tissera 2015; Lagos et al. 2017). In this context, discs form inside-out and, hence, the star formation (SF) starts in the central region and moves to the outskirts, contributing to set negative metallicity profiles (e.g. Chiappini, Matteucci & Romano 2001; Pilkington et al. 2012b; Tissera et al. 2016). The characteristics of the metallicity profiles provide insight into a variety of physical processes related to galaxy evolution, such as nucleosynthesis, stellar winds, SF and outflows, among others. These processes can change the oxygen abundance distribution of the interstellar medium (ISM) in a complex way, as each of them operates at different time- and space-scales. Additionally, secular evolution and radial migration, mergers and galaxy–galaxy interactions are dynamical processes that can also modify the distribution of chemical abundances in the ISM and the stellar populations (SPs), reshaping the metallicity profiles (Rupke, Kewley & Chien 2010; Amorín et al. 2012; Di Matteo 2016; Grand et al. 2016; Mollá et al. 2016; Tissera et al. 2016; Sillero et al. 2017; Ma et al. 2017; Tissera et al. 2019).

In the Local Universe, H II regions in spiral galaxies are known to have negative abundance gradients on average (e.g. Searle 1971; Martin & Roy 1992; Zaritsky, Kennicutt & Huchra 1994; Kennicutt, Bresolin & Garnett 2003; Rosales-Ortega et al. 2011), so that the inner regions are more metal-rich than the outskirts. However, departures from single metallicity gradients (Sánchez-Menguiano et al. 2017) and the existence of inverted metallicity gradients associated with interacting galaxies have been also reported (e.g. Rupke et al. 2010; Rosa et al. 2014). First observations of nearby spiral galaxies showed no clear indication of important azimuthal variations in the metallicity distributions (e.g. Kennicutt & Garnett 1996; Martin & Belley 1996; Cedrés & Cepa 2002; Cedrés et al. 2012; Li, Bresolin & Kennicutt 2013; Zinchenko et al. 2016). Only recently, with the help of integral field spectroscopic (IFS)

★ E-mail: patricia.tissera@unab.cl

surveys, has it been possible to analyse the metallicity distributions across the discs in more detail and with a larger statistical significance. Sánchez-Menguiano et al. (2017) analysed 63 face-on spiral galaxies selected from Calar Alto Legacy Integral Field Area (CALIFA) Survey data, finding differences in the chemical abundances of the arm and inter-arm regions, with modal values of -0.013 dex $R_{\rm eff}^{-1}$ and -0.015 dex $R_{\rm eff}^{-1}$ for flocculent and grand design spirals, respectively. Detailed observations of individual galaxies also provide evidence of azimuthal variations (Li et al. 2013; Sánchez-Menguiano et al. 2016; Ho et al. 2017; Vogt et al. 2017). For example, Ho et al. (2018) analysed the oxygen abundance of H II regions in NGC 2997, reporting ∼0.06 dex azimuthal variations in the oxygen abundance, with higher enrichment in the arm regions. Although the reported azimuthal variations are small, they provide information on the regulation of the SF activity and metal mixing process across the discs.

From a theoretical point of view, Grand et al. (2016) used high-resolution hydrodynamical simulations to follow the evolution of radial flows associated with the spiral arms. They showed how they could produce an overdensity of high-metallicity stars in the trailing side of the arms and an overdensity of metal-poor stars on the leading side. Di Matteo (2016) reported that radial migration induced by a bar can produce azimuthal variation of the old SPs using pure N-body simulations. Khoperskov et al. (2018) analysed the formation of azimuthal metallicity variations using high-resolution N-body simulations of discs with no initial metallicity gradients. They found that the different responses to a spiral perturbation of the kinematically hot and cold SPs produce variations in the metallicity distributions. Using analytical two-dimensional chemical models, Spitoni et al. (2019) study and quantify the effects of spiral arm density fluctuations on the azimuthal metallicity variations. They report an azimuthal variation of the metallicity gradients of the order of ∼0.1 dex.

Numerical simulations that include chemical models, such as the simulations from the Evolution and Assembly of GaLaxies and their Environment (EAGLE) Project (Crain et al. 2015; Schaye et al. 2015), are powerful tools to contsrain the subgrid models for the evolution of baryons. Chemical patterns give additional information both on the processes that regulate the SF activity and redistribute the angular momentum and mass in galaxies, and on the impact of inflows and outflows. Because they are not usually used to fix the free parameters of the algorithms of the subgrid physics, their analysis provide constraints to them. The chemical elements are often distributed within the nearby regions of the stellar sources (Mosconi et al. 2001). Unless other mechanisms are included, there will no further exchange of material within the minimum resolved volumes. Metal diffusion is expected to contribute to mitigate this issue, at the expense of introducing an extra free parameter – the metal diffusion coefficient (Greif et al. 2009; Pilkington et al. 2012a). The characteristics of the metal distribution and the gradients will be affected by the efficiency of the mixing and/or diffusion of chemical elements. This is an important issue, considering that the cooling rates depend strongly on the chemical abundances of the ISM, for example. The more detailed observational data that are being gathered by IFS surveys open up the possibility of performing more detail comparisons with models. Hence, we expect the analysis presented in this paper to serve as a benchmark for future improvements.

In this work, we analyse the azimuthal variation of oxygen abundances of the discs identified from a set of simulated galaxies extracted from the high-resolution (25 Mpc)^3 volume of the EAGLE Project. The EAGLE simulations have been proven to reproduce global properties of galaxies, such as the mass–metallicity relation (De Rossi et al. 2017), the fundamental relations of early-type galaxies (Lagos et al. 2018; Rosito et al. 2019; Trayford et al. 2019) and the locally resolved scale relation between SF and metallicity (Trayford & Schaye 2019), among others. In particular, these simulations provide a large sample of galaxies with different formation histories, which opens up the possibility of assessing the existence of azimuthal metallicity variations. This work is based on the galaxy catalogue built by Tissera et al. (2019) from which disc galaxies were selected for the higher-resolution run of a 25-Mpc cubic-side volume. In this paper, we analyse the azimuthal variations of the oxygen abundances in star-forming regions in the disc components at $z = 0$.

This paper is organized as follows. In Section 2, we describe the simulations and methods implemented to select the analysed SPs. In Section 3, we present the analysis of the azimuthal variations of the chemical abundance distributions. In Section 4, we study the metallicity profiles of stellar populations with higher and lower levels of enrichment. Finally, In Section 5, we summarize our main results. The Appendix provides information on the effect of the numerical dispersion on the metallicity distribution.

2 SIMULATIONS

The EAGLE Project[1] comprises cosmological hydrodynamical simulations consistent with a Λ-CDM universe, performed assuming $\Omega_\Lambda = 0.693$, $\Omega_{\rm m} = 0.307$, $\Omega_{\rm b} = 0.04825$, $h = 0.6777$ ($H_0 = 100$ h km s^{-1} Mpc^{-1}), $\sigma_8 = 0.8288$, $n_{\rm s} = 0.9611$ and $Y = 0.248$ (Ade et al. 2014). The simulations were performed with an enhanced version of the GADGET-2 code (Springel 2005) that includes a modified hydrodynamics solver and time stepping by the ANARCHY model (Schaller et al. 2015).

The code tracks the chemical enrichment of 11 chemical elements produced through mass loss by the intermediate-mass asymptotic giant branch and Type Ia and II supernovae as well as mass winds by massive stars (Wiersma et al. 2009b). A Chabrier initial mass function is adopted (Chabrier 2003). It also includes radiative cooling and a photo-heating model, as described in Wiersma, Schaye & Smith (2009a). The energy feedback model from stellar sources is implemented stochastically (Dalla Vecchia & Schaye 2012) and was calibrated to reproduce the stellar mass function and galaxy sizes at $z = 0$. More details of the simulations and the implemented subgrid physics can be found in Crain et al. (2015).

For this study, we use the re-calibrated simulation (Ref-L025N0752) representing a volume of 25 Mpc comoving box side, resolved by 752^3 initial particles. The mass resolution is 2.26×10^5 M$_\odot$ and 1.21×10^6 M$_\odot$ for the initial gas and dark matter particles, respectively. The maximum proper gravitational softening is 0.35 proper kpc.

The EAGLE Project also provides smoothed chemical abundances, which are estimated by applying a kernel function used to calculate smoothed values by using the information of the nearby regions. The smoothed abundances are used to estimate the cooling rates in the EAGLE simulations. Hence, in order to check their impact and for the sake of consistency, we repeated the whole analysis of the metallicity distributions by using the smoothed abundances in order to assess if the results depend on this mixing. We detect no significant change in the azimuthal variations or in the trends reported by using the non-smoothed abundances. Selected

[1]We use the publicly available data base of McAlpine et al. (2016).

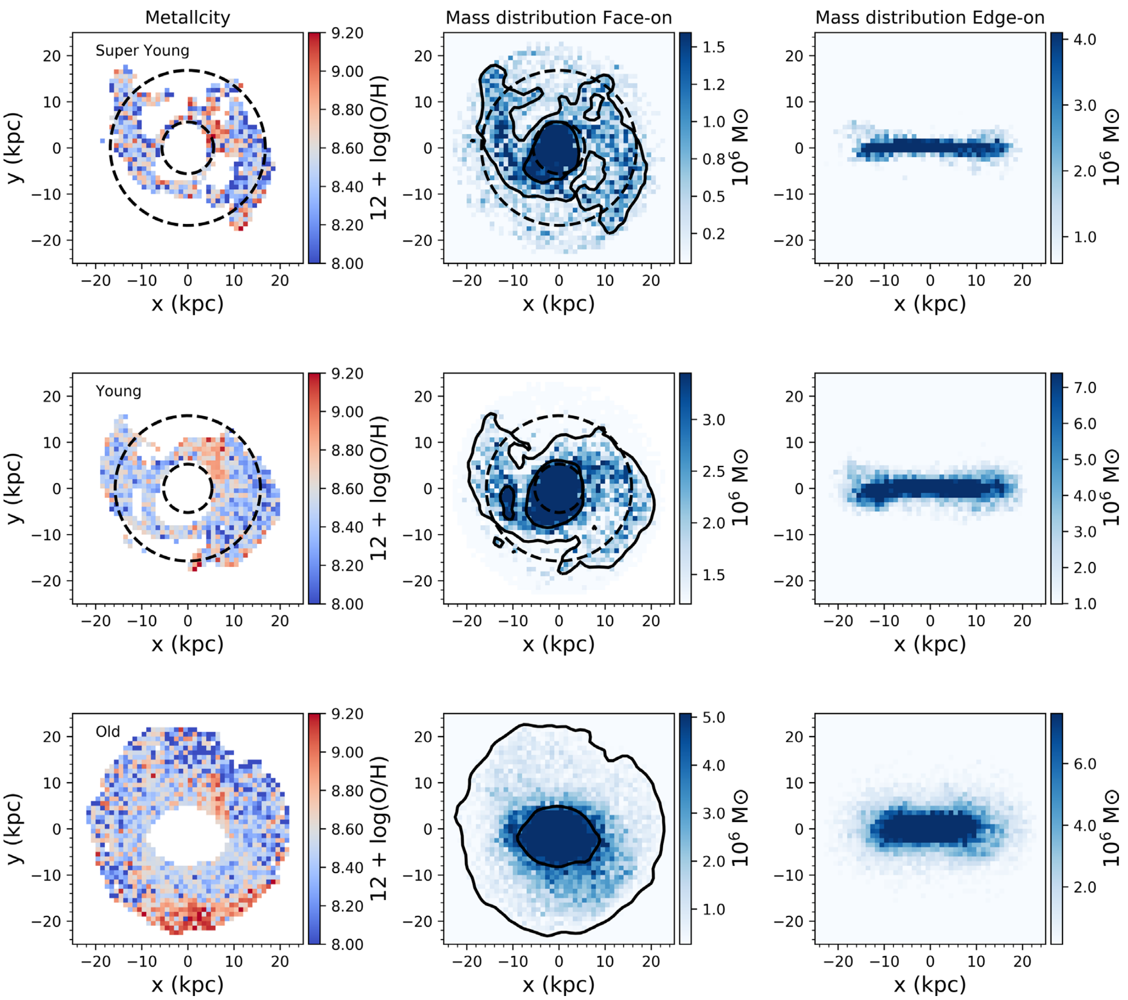

Figure 1. Metallicity and stellar mass distributions of a galaxy with well-defined spiral arms from our selected sample. Left panels: face-on projections of the oxygen abundance, 12 + log(O/H), for the super-young (top), young (middle) and old (bottom) SPs. Middle panels: face-on projections of stellar mass density of star particles for super-young (top), young (middle) and old (bottom) SPs. The inner and outer black circles represent 0.5 and 1.5 $R_{\rm eff}$, respectively. The black contours represent mass iso-densities chosen to highlight the arm and disc structures for young (top and middle) and old (bottom) SPs, respectively. The face-on metallicity projections were masked inside the mass iso-density contours shown in the middle panels. Right panels: the same as the middle panels but for edge-on projections of stellar mass density.

trends obtained using the smoothed abundances are included in the Appendix as examples.

2.1 Galaxy sample

The simulated galaxy sample is selected from the catalogue of Tissera et al. (2019), where the dynamical criteria based on the angular momentum context and binding energy were applied to identify the disc components (Tissera, White & Scannapieco 2012). The angular momentum content of each particle is quantified by $\epsilon = J_z/J_{z,\,\rm max}(E)$, where J_z is the angular momentum and $J_{z,\,\rm max}(E)$ is the maximum J_z over all particles at a given binding energy E. Only stars with $\epsilon > 0.5$ are taken into account to define the stellar disc component. Stars particles that are not rotationally supported are considered to belong to the spheroidal component and are not analysed in this work (see Rosito et al. 2019).

For the purpose of our analysis, we define two sets of SPs: young stars that are selected to have ages smaller than 2 Gyr, and super-young stars that are chosen to have ages younger than 0.5 Gyr. For each simulated galaxy, we estimate the star formation rate (SFR), the specific star formation rate (sSFR) and the half-mass radius ($R_{\rm eff}$), defined as the radius that encloses half the mass of the young (super-young) stellar discs. Galaxy morphology is defined by the ratio between the total stellar mass of the discs and the total stellar mass of a galaxy (D/T). The abundance ratio 12 + log(O/H) is used to quantify the level of enrichment of the simulated SPs (hereafter, we also use the term 'metallicity' to refer to the oxygen abundances).

We follow previous works that have shown that young SPs can be taken as tracers of the chemical abundances of the star-forming regions in the ISM (Gibson et al. 2013; Tissera et al. 2016). We adopt the same criteria considering the two above-mentioned age thresholds, which are used for different aspects of the analysis. Only those discs with more than 1000 young (super-young) stars are analysed. This condition is adopted because the estimation of the metallicity gradients in different azimuthal directions requires us to be able to numerically resolve all of them with a suitable number of star particles. The final samples comprise 106 and 42 discs (sampled by young stars and super-young stars, respectively). The selected galaxies have stellar masses in the range $[10^9, 10^{10.8}]$ $\rm M_\odot$ and SFRs in range $[0.1, 6]\,\rm M_\odot\,yr^{-1}$.

In order to illustrate the distribution of both metallicity and mass of the SPs studied, Fig. 1 shows the face-on projections of metallicity (left panels) and the face-on (middle panels) and edge-on (right panels) projections of the stellar mass density for the super-young, young and old (with ages >2 Gyr) SPs. To create these maps, we used grids of 50 × 50 pixel^2 on images with a physical size of 50 × 50 kpc^2. For the face-on metallicity projection, each pixel was assigned the median value along the z-axis, while for the face-on and edge-on stellar mass density projections, the sum of the stellar mass along the z- and y-axes, respectively, was assigned. As expected, both super-young and young SPs are good tracers of the spiral arms, as denoted by the iso-density contours on the face-on images and they are distributed in a thin disc, as shown in edge-on projections, while the old SP traces the disc and is distributed in a thick disc (see face-on and edge-on projections, respectively). The metallicity distributions of super-young and young SPs have larger contributions of high-metallicity SPs (12 + log(O/H) > 8.5; red points), while the old SPs seem to have more homogeneous values around of 12 + log(O/H) ∼ 8.5 (white points). The different spatial and numerical distributions of metallicity among the SPs are quantified in more detail in the following sections.

3 AZIMUTHAL VARIATIONS OF THE OXYGEN PROFILES

In this section, we quantify the azimuthal variations of the oxygen abundance gradients by estimating the metallicity profiles along different directions on the disc plane from an observer located at the galactic centre. Each galaxy is rotated so that the total angular momentum is located along the z-axis. The stellar discs are projected along the z-axis. For simplicity, the azimuthal variations are obtained by tessellating, in six equal subregions, the projected stellar mass distributions, along the main axis of rotation. Each of the resulting regions covers 60° of the total disc (360°). The radial metallicity profiles are obtained by estimating the median oxygen abundance values in radial intervals, each enclosing the same number of star particles.[2] We only considered subregions with at least 200 young SPs, so each had enough star particles to estimate the metallicity profiles. In order to have enough SPs in each subregion, in this section, we work with the young SPs (ages <2 Gyr).

Linear regression fittings to the metallicity profiles are constructed by applying the least trimmed squares (LTS) robust method that considers errors in the y-variable, leaving out possible outliers (Rousseeuw & Van Driessen 2006; Cappellari et al. 2013). The errors correspond to three times the bootstrap errors estimated for each radial interval.[3] A linear regression of the form, $y = b(x - x_0) + a$, is used in all cases. It should be noted that the metallicity profiles are normalized by $R_{\rm eff}$, before applying the LTS fits over the radial range $[0.5, 1.5]R_{\rm eff}$.

After this procedure, six slopes (∇) and six zero-points (ZP) for each galaxy are obtained. We estimated the zero-points at the interception with $x = 0$. The median azimuthal slopes ($\nabla_{\rm M}$) and zero-points ($ZP_{\rm M}$) were estimated from the linear regressions calculated for the six subregions. Their respective standard deviations are obtained by applying a bootstrap technique (σ_∇ and σ_{ZP}). Additionally, the overall metallicity gradients were also calculated by using concentric radial averages ($\nabla_{\rm T}$ and $ZP_{\rm T}$). In summary, for each simulated galaxy, we have four parameters: $\nabla_{\rm T}$, σ_∇, $ZP_{\rm T}$ and σ_{ZP}.

Fig. 2 shows the metallicity profiles obtained for each of the six subregions of a typical simulated disc (black dashed lines) compared with the overall metallicity profile for the whole disc (red solid lines) as an example. As can be seen from Fig. 2, there are clear azimuthal variations of the slopes and zero-points of the metallicity profiles of each subregion.

Fig. 3 displays the metallicity gradients and zero-points estimated along one of the defined azimuthal subsamples selected at random, $\nabla_{\rm Random}$ and $ZP_{\rm Random}$, as a function of $\nabla_{\rm T}$ and $ZP_{\rm T}$. The gradient and zero-point of the metallicity profiles taken at random from our set of six directions correlate with those obtained from the radial averages over the whole discs, indicating that even if there are azimuthal variations, the information store in the overall profiles can be recovered by using measures along a certain direction. However, as can be seen from this figure, both relations show large dispersion. The Spearman coefficients of the correlations are $r \sim 0.46$ and $r \sim 0.43$ for the slopes and zero-points, respectively. This suggests that the azimuthal variations are significant.

The relation between the azimuthal dispersions of the slopes σ_∇ and those of the zero-points σ_{ZP} is depicted in Fig. 4. As can be seen, there is a trend for discs with larger σ_∇ to also have larger azimuthal variations of the zero-point. The error bars are estimated by using a bootstrap technique. The median values are $\sigma_\nabla \sim 0.12 \pm 0.03$ dex $R_{\rm eff}^{-1}$ and $\sigma_{ZP} \sim 0.12 \pm 0.03$ dex.

To explore the origin of the azimuthal variation of the metallicity profiles, Fig. 5 shows σ_∇ and σ_{ZP} as a function of D/T (upper panels), $R_{\rm eff}$ (middle panels) and log SFR (lower panels) coloured by $\nabla_{\rm T}$ (left panels) and $ZP_{\rm T}$ (right panels). The median values and the 25th and 75th percentiles (error bars) are also included. We find weak trends of the azimuthal dispersions in the gradients as a function of D/T and SFR. These indicate slightly higher azimuthal variations of the metallicity distributions in discs of more bulge-dominated systems and low SFR galaxies. We would like to point out that the larger azimuthal variation of the metallicity distributions detected for galaxies with low SF activity could also be affected by the numerical resolution, and hence these trends should be confirmed by using higher-resolution simulations. No clear trend is found for the azimuthal variations of the zero-points of the metallicity profiles. There are no clear trends for both dispersions with $R_{\rm eff}$.

The fact that disc-dominated galaxies show less azimuthal dispersion in the metallicity gradients could be associated with their more quiescent evolution history where the ISM became progressively enriched and the stellar distributions were not strongly disturbed. However, bulge-dominated galaxies had a larger probability of having experienced mergers or interactions in the past, as shown by Tissera et al. (2019). We speculate that these mechanisms could have disturbed the stellar distributions and, hence, increased the azimuthal dispersion, forming a bar, for example. The impact would depend on the merger/interaction parameters and how close in time from $z \approx 0$ these events had taken place. A more detailed analysis of possible mixing processes would require better space and temporal resolutions. Well-defined disc galaxies ($D/T \geq 0.5$) in the EAGLE simulations have azimuthal variations in the metallicity gradients of

[2] A total of 20 radial intervals are defined in each disc resolved with N particles, within $[0.5, 1.5]R_{\rm eff}$. The interval widths are determined by the distributions of n particles, where $n = N/20$.

[3] Bootstrap errors are used instead of the standard dispersion in each interval because the analysis of the metallicity distributions shows that the dispersions have a systematic skewness with a lower metallicity tail at all radii.

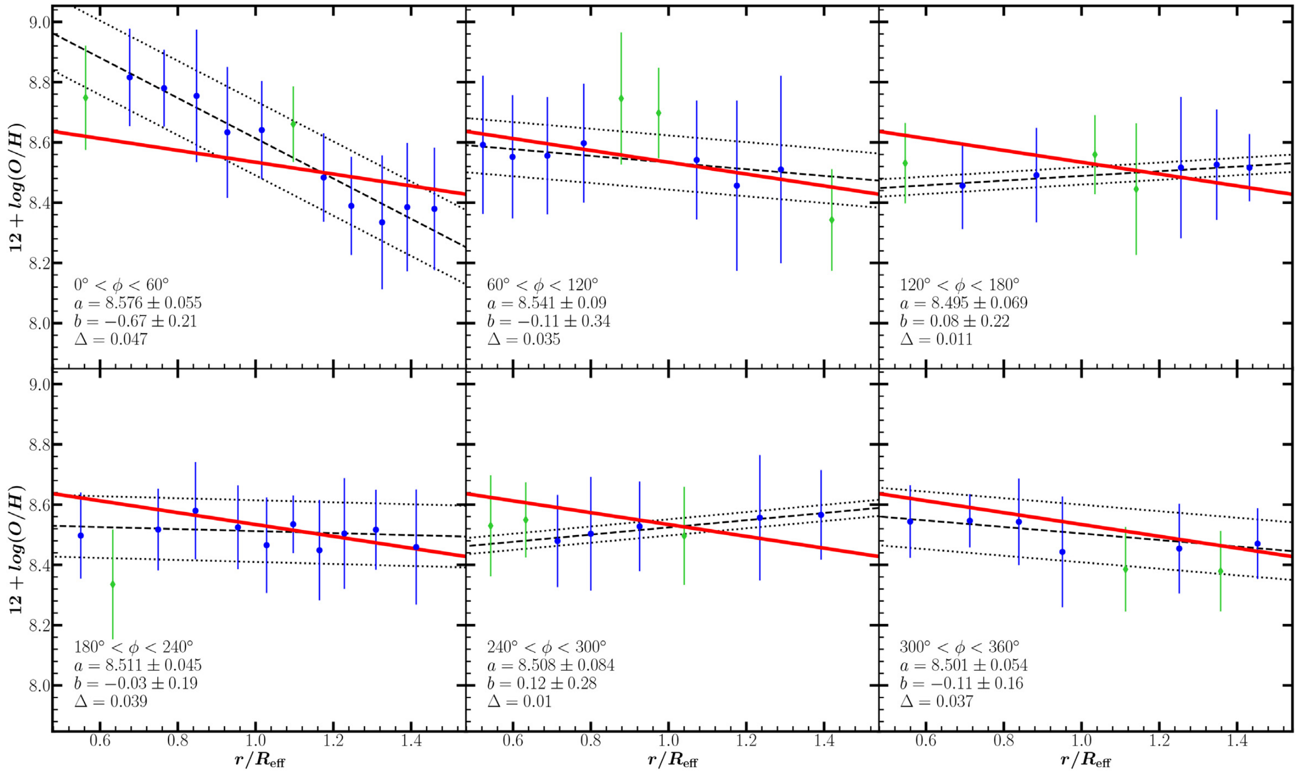

Figure 2. Oxygen abundance profiles of the SF regions located in each of the six subregions defined to assess the azimuthal variations for a typical galaxy (black dashed lines). The error bars denote three times the bootstrap errors. For comparison, the global averaged profile is also shown (red thick line). The standard metallicity deviations in each radial average are included (only blue points are considered for the LTS fits while green symbols are classified as outliers; Rousseeuw & Van Driessen 2006; Cappellari et al. 2013). The black dotted lines are the linear fits of LTS ± 2.6Δ (standard deviation).

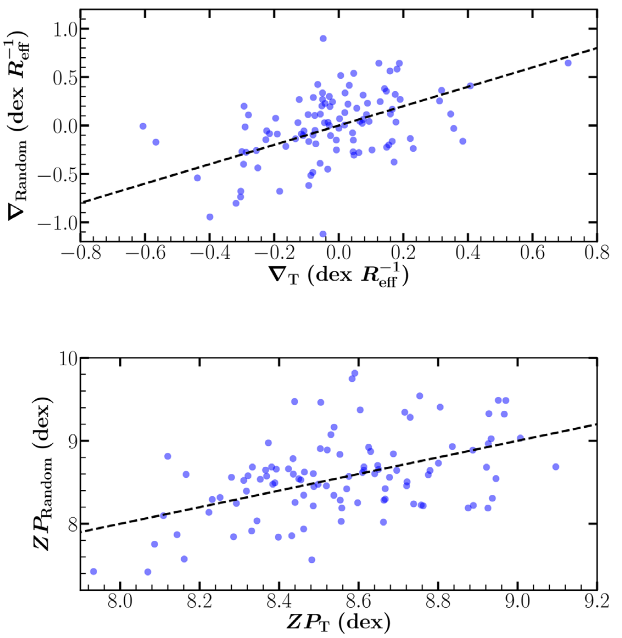

Figure 3. Metallicity gradient $\nabla_{\rm Random}$ estimated along an azimuthal subsample selected at random from the six defined subregions as a function of the global metallicity slopes $\nabla_{\rm T}$ (upper panel) and the corresponding zero-points $ZP_{\rm Random}$ as a function of the global ones $ZP_{\rm T}$ (lower panel).

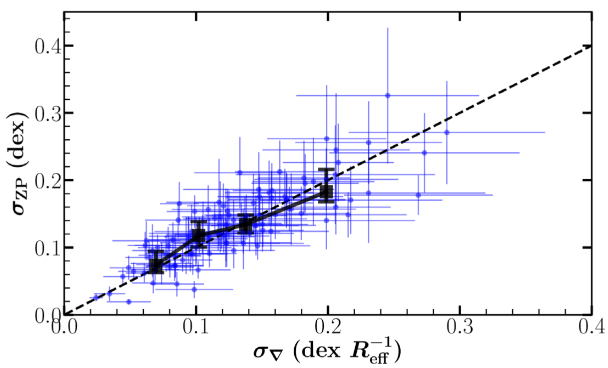

Figure 4. Median values of the standard deviations of the azimuthal zero-points σ_{ZP} as a function of those of σ_{∇} (black squares). The black error bars represent the 25th and 75th percentiles. The blue small dots and blue error bars represent the data for individual simulated galaxies and the corresponding errors obtained by applying a bootstrap sampling technique over the six azimuthal subregions.

$\sim$0.1 dex $R_{\rm eff}$. This value is in agreement with the results reported by Spitoni et al. (2019) for spirals using a chemo-dynamical model.

4 OXYGEN PROFILES IN ARM AND INTER-ARM REGIONS

Another approach to the study of azimuthal metallicity variations is to analyse the residual metallicity distributions. With the super-

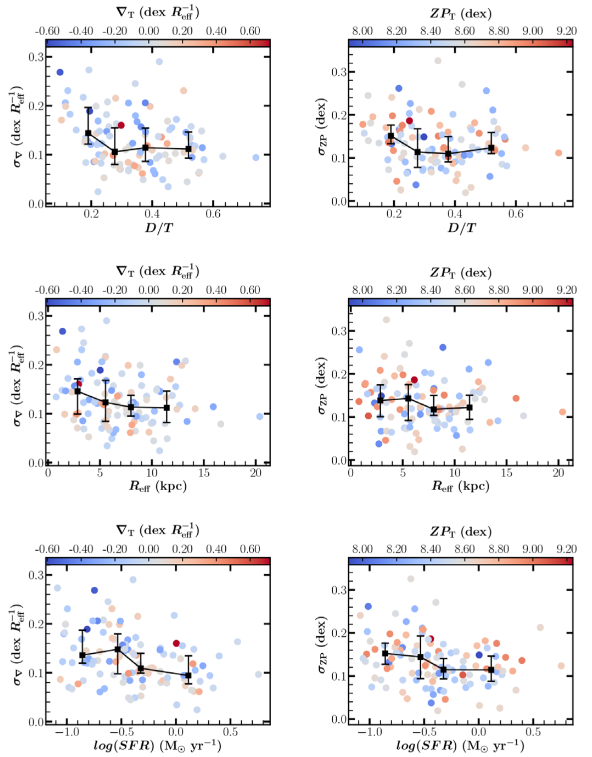

Figure 5. σ_∇ (left panels) and σ_{ZP} (right panels) as a function of *D*/*T* (upper panel), R_{eff} (middle panel) and SFR (lower panel). The colour bars show ∇_T (left panels) and ZP_T (left panels). Median values are shown (black squares) with error bars representing the 25th and 75th percentiles.

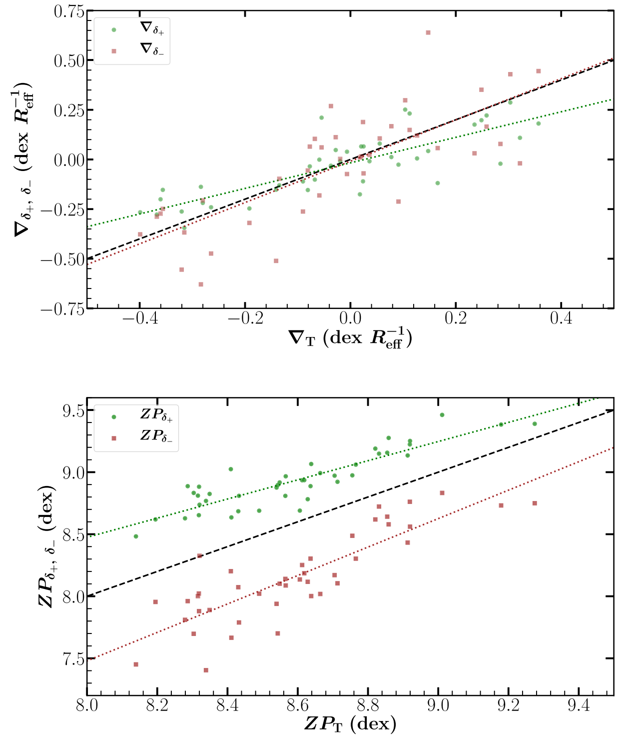

Figure 6. Upper panel: ∇_{δ_+} (green dots) and ∇_{δ_-} (red squares) as a function of ∇_T estimated for the whole distribution of super-young SPs. Lower panel: ZP_+ (green dots) and ZP_- (red squares) as a function of ZP_T. The black dashed line corresponds to a 1 : 1 relation in both plots.

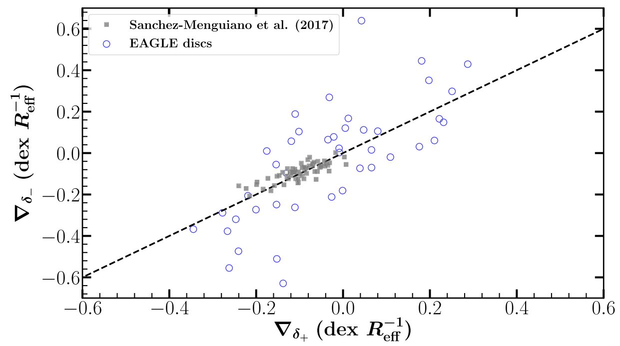

Figure 7. ∇_{δ_+} as a function of ∇_{δ_-} defined by super-young SPs (blue circles). The black dashed line corresponds to the 1 : 1 relation. Observations form Sánchez-Menguiano et al. (2017) have been included only for reference (grey points) as they estimated the gradients using selected H II regions located in the arm and inter-arm regions.

young SPs, we estimate the overall metallicity profiles and obtain ∇_T and ZP_T, following the same procedure explained in the previous section. Then, the SPs that have an excess or deficit of oxygen abundances with respect to the overall metallicity profile are identified by defining the residues (δ):

$$\delta(r_i) = Z_{real}(r_i) - Z_{fit}(r_i). \qquad (1)$$

Here, $Z_{real}(r_i)$ is the metallicity of a given super-young SP located at a galactocentric distance r_i and $Z_{fit}(r_i)$ is the metallicity it should have at that r_i, according to the overall linear fit. We note that this procedure is applied to all selected stars in order to build up the metallicity residual maps. We choose to use the fitting relations as reference values because this is the usual way of quantifying the metallicity distributions at any redshift (Carton et al. 2018) and they allow us to have a reference value to define the residuals for each individual SP. Hence, each super-young SP is classified as having a metallicity excess (δ_+) or deficit (δ_-) with respect to the overall level of enrichment. The radial metallicity profiles of the super-young SPs with δ_+ and δ_- are estimated following the same procedure explained in the previous section (∇_{δ_+} and ZP_{δ_+} and ∇_{δ_-} and ZP_{δ_-}, respectively). In Fig. 6, we show the gradients and zero-points determined by the regions with excess versus those with deficit with respect to the overall metallicity profiles. As can be appreciated, there is a slight trend for the regions with excess metallicity to show weaker gradients. From this figure, we can see a systematic shift for the zero-point values of the excess and deficit profiles, with respect to the ZP_T of the global metallicity profiles. The difference between the zero-points of the regions with excess and deficit metallicities with respect to the median values is smaller for the galaxies with higher metallicity. This suggests a higher mixing of chemical elements or/and a prolonged SF history.

Fig. 7 shows the relation of ∇_{δ_-} versus ∇_{δ_+} together with the metallicity gradients reported by Sánchez-Menguiano et al. (2017), which are displayed for the sake of comparison. However, it is important to stress that the latter were obtained by applying a different method. Sánchez-Menguiano et al. (2017) estimated the metallicity gradients for H II regions located in the arm and inter-arm regions. Nevertheless, both approaches intend to highlight the differences in the metallicity distributions of the SPs in the discs. It is clear that the simulated parameters show large dispersion, which, at least in part, could be due to inefficient mixing of the chemical elements or more clumpy SF activity.

In order to complete the analysis, we explore if the smoothed abundances could reduce the scatter by repeating this analysis with the smoothed element abundances, as shown in the Appendix. As can be seen from Fig. A2, using the smoothed abundances does not reduce the scatter in the metallicity gradients or reduce the gap between the level of enrichment between the SPs classified as having metallicity excess or deficit.

5 CONCLUSIONS

We study the azimuthal variation of the oxygen abundances of young and super-young SPs, which can be used as tracers of the regions of active SF in the discs of galaxies selected from the higher-resolution run of the EAGLE Project, Ref-L025N0752. The azimuthal variations of the metallicities can store information on the evolution of discs and, currently, IFS observations provide detail information of the metallicity distributions. Additionally, they provide another route to confront the subgrid physics with observations. Our analysed sample is composed of 106 (42) galaxies resolved with at least 1000 young (super-young) star particles. As a consequence, our sample represents star-forming galaxies with SFR $> 0.1\ \mathrm{M_\odot\ yr^{-1}}$.

Our main results can be summarized as follows.

(i) Although we find a correlation between the metallicity gradients measured along a random direction and those estimated by using global averages over the discs, the scatter is large enough to suggest that azimuthal variations are significant. The azimuthal dispersion of the slopes and zero-points of young stars in the EAGLE discs are found to be around 0.12 ± 0.03 dex $R_{\rm eff}^{-1}$ and 0.12 ± 0.03 dex, respectively.

(ii) A weak trend of larger metallicity azimuthal dispersions is detected for galaxies with lower SF activity and $D/T < 0.2$. The larger variation for bulge-dominated galaxies and low SF activity is in agreement with the results obtained by Tissera et al. (2019), where the gas-phase oxygen profiles in the SF regions were analysed for galaxies of different morphologies in the EAGLE simulations. Previous works reported bulge-dominated systems to have a greater frequency of mergers. These events could have destroyed part of the discs or disturbed them by forming bar or spiral structures, which could have contributed to mix up the SPs. It should also be considered that these systems have lower SF activity and, even though we required a minimum number of stars to make the estimations, the dispersion could be more affected by the numerical resolution than those discs with larger SFRs. However, currently, it is still difficult to have a large data set of galaxies with a vast variety of morphologies and, at the same time, with high numerical resolution. Well-defined discs with $D/T > 0.4$ show azimuthal dispersions of $\sim 0.1 \mathrm{dex/R_{eff}}$, in good agreement with the predictions by Spitoni et al. (2019). We find no clear trends with $R_{\rm eff}$.

(iii) The metallicity slopes estimated using the super-young SPs with metallicity excess are slightly shallower than the overall estimations. However, the larger variation of these gradients in the simulations with respect to the current observations (e.g. Sánchez-Menguiano et al. 2016) suggests the relevance of exploring in more detail the flow of metals at subgalactic scales.

ACKNOWLEDGEMENTS

The authors thank A. Benitez-Llambay and J. Schaye for useful comments. JAHJ thanks CONICYT, Programa de Astronomía, Fondo ALMA-CONICYT 2017, Código de proyecto 31170038. PBT acknowledges partial funding by Fondecyt Regular 2015–1150334 and Internal Project Unab 2019. This project has received funding from the European Union Horizon 2020 Research and Innovation Programme under the Marie Sklodowska-Curie grant agreement No 734374. This work used the RAGNAR cluster funded by Fondecyt 1150334 and Universidad Andres Bello. This work used the DiRAC Data Centric system at Durham University, operated by the Institute for Computational Cosmology on behalf of the STFC DiRAC HPC Facility (www.dirac.ac.uk). This equipment was funded by BIS National E-infrastructure capital grant ST/K00042X/1, STFC capital grants ST/H008519/1 and ST/K00087X/1, STFC DiRAC Operations grant ST/K003267/1 and Durham University. DiRAC is part of the National E-Infrastructure. We acknowledge PRACE for awarding us access to the Curie machine based in France at TGCC, CEA, Bruyeres-le-Chatel.

REFERENCES

Ade P. A. R. et al., 2014, A&A, 571, A1
Amorín R., Vílchez J. M., Hägele G. F., Firpo V., Pérez-Montero E., Papaderos P., 2012, ApJ, 754, L22
Cappellari M. et al., 2013, MNRAS, 432, 1709
Carton D. et al., 2018, MNRAS, 478, 4293
Cedrés B., Cepa J., 2002, A&A, 391, 809
Cedrés B., Cepa J., Bongiovanni Á., Castañeda H., Sánchez-Portal M., Tomita A., 2012, A&A, 545, A43
Chabrier G., 2003, ApJ, 586, L133
Chiappini C., Matteucci F., Romano D., 2001, ApJ, 554, 1044
Crain R. A. et al., 2015, MNRAS, 450, 1937
Dalla Vecchia C., Schaye J., 2012, MNRAS, 426, 140
De Rossi M. E., Bower R. G., Font A. S., Schaye J., Theuns T., 2017, MNRAS, 472, 3354
Di Matteo P., 2016, PASA, 33, e027
Fall S. M., Efstathiou G., 1980, MNRAS, 193, 189
Gibson B. K., Pilkington K., Brook C. B., Stinson G. S., Bailin J., 2013, A&A, 554, A47
Grand R. J. J. et al., 2016, MNRAS, 460, L94
Greif T. H., Glover S. C. O., Bromm V., Klessen R. S., 2009, MNRAS, 392, 1381
Ho I. T. et al., 2017, ApJ, 846, 39
Ho I. T. et al., 2018, A&A, 618, A64
Kennicutt R. C. J., Garnett D. R., 1996, ApJ, 456, 504
Kennicutt R. C. J., Bresolin F., Garnett D. R., 2003, ApJ, 591, 801
Khoperskov S., Di Matteo P., Haywood M., Combes F., 2018, A&A, 611, L2
Lagos C. d. P., Theuns T., Stevens A. R. H., Cortese L., Padilla N. D., Davis T. A., Contreras S., Croton D., 2017, MNRAS, 464, 3850
Lagos C. d. P. et al., 2018, MNRAS, 473, 4956
Li Y., Bresolin F., Kennicutt R. C. J., 2013, ApJ, 766, 17
Ma X., Hopkins P. F., Wetzel A. R., Kirby E. N., Anglés-Alcázar D., Faucher-Giguère C.-A., Kereš D., Quataert E., 2017, MNRAS, 467, 2430
McAlpine S. et al., 2016, Astronomy and Computing, 15, 72
Martin P., Belley J., 1996, ApJ, 468, 598
Martin P., Roy J.-R., 1992, ApJ, 397, 463
Mollá M., Díaz Á. I., Gibson B. K., Cavichia O., López-Sánchez Á.-R., 2016, MNRAS, 462, 1329
Mosconi M. B., Tissera P. B., Lambas D. G., Cora S. A., 2001, MNRAS, 325, 34
Pedrosa S. E., Tissera P. B., 2015, A&A, 584, A43
Pilkington K. et al., 2012a, MNRAS, 425, 969
Pilkington K. et al., 2012b, A&A, 540, A56

Rosa D. A., Dors O. L., Krabbe A. C., Hägele G. F., Cardaci M. V., Pastoriza M. G., Rodrigues I., Winge C., 2014, MNRAS, 444, 2005
Rosales-Ortega F. F., Díaz A. I., Kennicutt R. C., Sánchez S. F., 2011, MNRAS, 415, 2439
Rosito M. S., Tissera P. B., Pedrosa S. E., Rosas-Guevara Y., 2019, A&A , 629, A37
Rousseeuw P. J., Van Driessen K., 2006, Data Mining and Knowledge Discovery, 12, 29
Rupke D. S. N., Kewley L. J., Chien L. H., 2010, ApJ, 723, 1255
Sánchez-Menguiano L. et al., 2017, A&A, 603, A113
Sánchez-Menguiano L. et al., 2016, ApJ, 830, L40
Schaller M., Dalla Vecchia C., Schaye J., Bower R. G., Theuns T., Crain R. A., Furlong M., McCarthy I. G., 2015, MNRAS, 454, 2277
Schaye J. et al., 2015, MNRAS, 446, 521
Searle L., 1971, ApJ, 168, 327
Sillero E., Tissera P. B., Lambas D. G., Michel-Dansac L., 2017, MNRAS, 472, 4404
Spitoni E., Cescutti G., Minchev I., Matteucci F., Silva Aguirre V., Martig M., Bono G., Chiappini C., 2019, A&A , 628, A38
Springel V., 2005, MNRAS, 364, 1105
Tissera P. B., White S. D. M., Scannapieco C., 2012, MNRAS, 420, 255
Tissera P. B., Pedrosa S. E., Sillero E., Vilchez J. M., 2016, MNRAS, 456, 2982
Tissera P. B., Rosas-Guevara Y., Bower R. G., Crain R. A., del P Lagos C., Schaller M., Schaye J., Theuns T., 2019, MNRAS, 482, 2208
Trayford J. W., Schaye J., 2019, MNRAS, 485, 5715
Trayford J. W., Frenk C. S., Theuns T., Schaye J., Correa C., 2019, MNRAS, 483, 744
Vogt F. P. A., Pérez E., Dopita M. A., Verdes-Montenegro L., Borthakur S., 2017, A&A, 601, A61
Wiersma R. P. C., Schaye J., Smith B. D., 2009a, MNRAS, 393, 99
Wiersma R. P. C., Schaye J., Theuns T., Dalla Vecchia C., Tornatore L., 2009b, MNRAS, 399, 574
Zaritsky D., Kennicutt Robert C. J., Huchra J. P., 1994, ApJ, 420, 87
Zinchenko I. A., Pilyugin L. S., Grebel E. K., Sánchez S. F., Vílchez J. M., 2016, MNRAS, 462, 2715

APPENDIX: ANALYSIS OF THE METALLICITY DISPERSION

The EAGLE Project provides smoothed variables of the chemical abundances estimated by using the kernel function adopted for the Smoothed Particle Hydrodynamics calculations. These smoothed variables are estimated at the time the stars are formed. They provide a rough estimation of the effects that a more efficient mixing process might have. We re-do all the calculations to assess if the trend changed when the smoothed abundances are used instead of the non-smoothed variables. However, no significant or systematic differences are found. As an example, in Fig. A1, we show the median dispersion in the slope and zero-point of the metallicity gradients for both cases. Similarly, in Fig. A2, we show the slope and zero-points obtained by using the SF regions with excess or deficit metallicity with respect to the corresponding averages. As can be seen, there are no statistical differences between the results obtained from both relations.

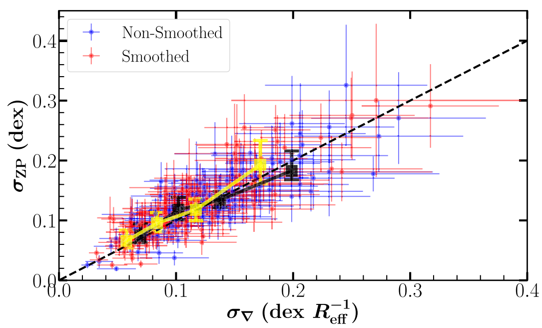

Figure A1. Median values of the standard deviations of the azimuthal zero-points, σ_{ZP}, as a function of those of the slopes, σ_∇, for the non-smoothed (black squares) and smoothed (yellow squares) metallicity profiles. The black (yellow) error bars represent the 25th and 75th percentiles of the non-smoothed (smoothed) relations. The blue (red) small dots and blue (red) error bars represent the data for individual simulated galaxies and the corresponding errors obtained by applying a bootstrap sampling technique over the six azimuthal subregions.

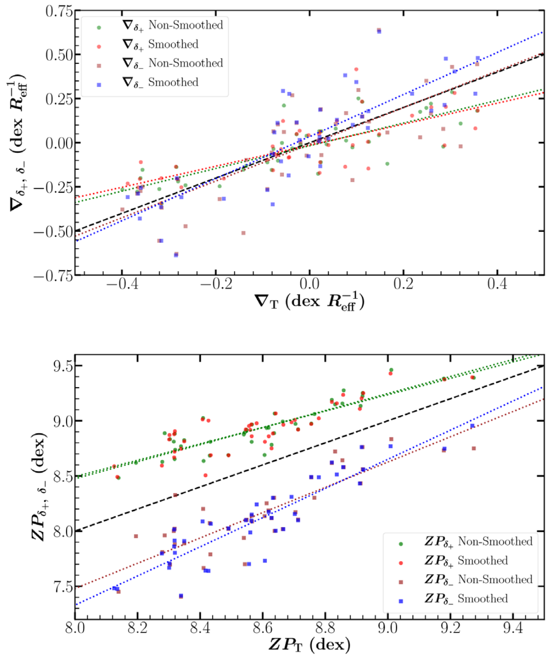

Figure A2. Upper panel: ∇_{δ_+} and ∇_{δ_-} as a function of $\nabla_{\rm T}$ estimated for the whole distribution of super-young SPs using the non-smoothed and smoothed chemical abundances. The black dashed line represents the 1 : 1 relation. The dashed lines depict linear regressions to the distributions of ∇_{δ_+} and ∇_{δ_-} for the smoothed and non-smoothed relations. Lower panel: ZP_+ and ZP_- as a function of $ZP_{\rm T}$. The black dashed lines represent a 1 : 1 relation, for comparison purposes.

This paper has been typeset from a TEX/LATEX file prepared by the author.